Quantum Superinductor with Tunable Nonlinearity

M. T. Bell, I. A. Sadovskyy, L. B. Ioffe, A. Yu. Kitaev, and M. E. Gershenson

Phys. Rev. Lett. **109**, 137003 — Published 27 September 2012

DOI: 10.1103/PhysRevLett.109.137003

Quantum Superinductor with Tunable Non-Linearity

M.T. Bell,[1] I.A. Sadovskyy,[1] L.B. Ioffe,[1] A.Yu. Kitaev,[2] and M.E. Gershenson[1]
[1] *Department of Physics and Astronomy, Rutgers University, Piscataway, NJ 08854, USA and*
[2] *Caltech, Institute for Quantum Information, Pasadena, CA 91125, USA*

We report on the realization of a superinductor, a dissipationless element whose microwave impedance greatly exceeds the resistance quantum R_Q. The design of the superinductor, implemented as a ladder of nanoscale Josephson junctions, enables tuning of the inductance and its non-linearity by a weak magnetic field. The Rabi decay time of the superinductor-based qubit exceeds $1\,\mu$s. The high kinetic inductance and strong non-linearity offer new types of functionality, including the development of qubits protected from both flux and charge noises, fault tolerant quantum computing, and high-impedance isolation for electrical current standards based on Bloch oscillations.

PACS numbers: 74.50.+r, 74.81.Fa, 85.25.Am

Superinductors are desired for the implementation of the electrical current standards based on Bloch oscillations [1, 2], protection of Josephson qubits from the charge noise [3, 4], and fault tolerant quantum computation [5, 6]. The realization of superinductors poses a challenge. Indeed, the "geometrical" inductance of a wire loop is accompanied by a sizable parasitic capacitance, and the loop impedance Z does not exceed αR_Q [7], where $\alpha = 1/137$ is the fine structure constant and $R_Q = h/4e^2$ is the resistance quantum. This limitation does not apply to superconducting circuits whose kinetic inductance L_K is associated with the inertia of the Cooper pair condensate [8].

The kinetic inductance of a Josephson junction, $L_K = (\Phi_0/2\pi)^2/E_J$, scales inversely with its Josephson energy E_J [8] ($\Phi_0 = h/2e$ is the flux quantum). The kinetic inductance can be increased by reducing the in-plane junction dimensions and, thus, E_J. However, this resource is limited: with shrinking the junction size, the charging energy $E_C = e^2/2C$ (C is the junction capacitance) increases and the phase slip rate $\propto \exp[-(8E_J/E_C)^{1/2}]$ [8] grows exponentially, which leads to decoherence. Small Josephson energy (i.e. large kinetic inductance) can be realized in chains of dc SQUIDs frustrated by the magnetic field [9, 10]. However, the phase slip rate increases greatly with frustration, and the chains do not provide good isolation from the environment. For the linear chains of Josephson junctions with $E_J/E_C \gg 1$, relatively large values of L_K (up to 300 nH [3]) have been realized in the phase-slip-free regime; further increase of the impedance of these chains is hindered by the growth of their parasitic capacitance. Also, the linear chains, as well as the nanoscale superconducting wires with a kinetic inductance of $\sim 10\,\mathrm{nH}/\mu\mathrm{m}$ [11, 12], are essentially linear elements whose inductance is not readily tunable (unless large currents are applied).

We propose a novel superinductor design that has several interesting features. This circuit can be continuously tuned by a weak magnetic field between the regimes characterized by a low linear inductance and a very large non-linear inductance. Importantly, the large impedance $Z \gg R_Q$ is realized when the decoherence processes associated with phase slips are fully suppressed. This combination of strong non-linearity and low decoherence rate is an asset for the development of high-performance superconducting qubits and controllable coupling between qubits.

The studied circuit is a "ladder" of nanoscale Josephson junctions frustrated by the magnetic flux Φ [Fig. 1(a)]. Each unit cell of the ladder represents an asymmetric dc-SQUID with a single "small" junction with the Josephson energy E_{JS} in one arm and three "large" Josephson junctions with the Josephson energy E_{JL} in the other arm (the in-plane dimensions of both types of tunnel junctions do not exceed $0.3 \times 0.3\,\mu\mathrm{m}^2$). The adjacent cells are coupled via one large junction; the Josephson energy of the system, $E_J(\varphi)$, remains an even function of the phase difference φ across the ladder at any value of the flux (the benefits of this symmetry are discussed below).

For the Josephson junctions in the ladder "backbone", the Josephson energy is two orders of magnitude larger than the charging energy (the junction parameters are summarized in Table I). In this case quantum fluctuations of the phase across individual junctions are small, and the dependence $E_J(\varphi)$ (see Fig.1b) can be obtained from the classical computation that minimizes E_J with respect to the phases of superconducting islands at a fixed φ. At zero frustration ($\Phi = 0$) the energy $E_J(\varphi)$ is approximately parabolic over the relevant range of φ. With an increase of the magnetic field, the curvature of $E_J(\varphi)$ near $\varphi = 0$ decreases. Provided the ratio of the Josephson energies for large and small junctions, $r = E_{JL}/E_{JS}$, is not too large, the curvature $\partial^2 E_J(\varphi)/\partial\varphi^2|_{\varphi=0}$ vanishes at some critical flux Φ_c. At this frustration the potential is strongly anharmonic (approximately quartic) and the kinetic inductance, which is inversely proportional to the curvature of the potential $L_K \propto [\partial^2 E_J(\varphi)/\partial\varphi^2]^{-1}$ [8] in its minimum, diverges.

The optimal regime of operation for the studied su-

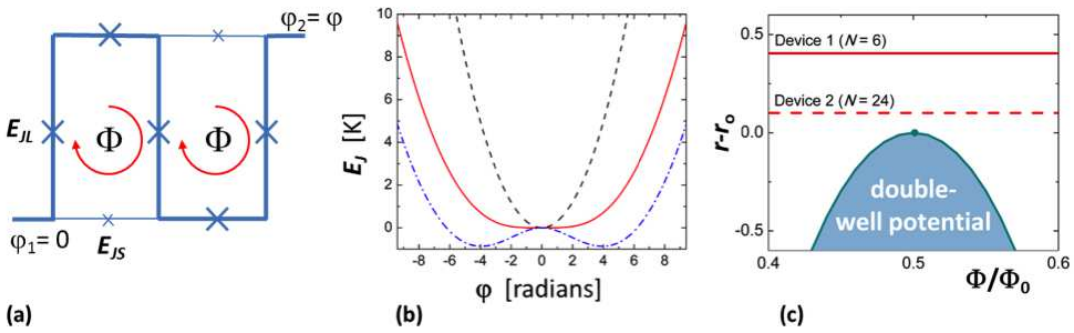

FIG. 1: (Color online) Superinductor unit cells, potential energy, and phase diagram. (a) The unit cells of the tested device include "small" and "large" Josephson junctions with Josephson energies $E_{\rm JS}$ and $E_{\rm JL}$, respectively. The "backbone" of the superinductor is shown as a bold line; the adjacent cells share large Josephson junctions. The cells are threaded by the same magnetic flux Φ; the phase difference across the device is $\varphi_2 - \varphi_1 = \varphi$. (b) The Josephson energy $E_{\rm J}(\varphi)$ of a six-cell ladder calculated within the quasi-classical approximation at $\Phi = 0$ (dashed curve) and $\Phi = \Phi_0/2$ (solid and dash-dotted curves); $E_{\rm JS} = 3.5\,{\rm K}$ for all three curves, $E_{\rm JL} = 16.8\,{\rm K}$ for dashed and solid curves and $E_{\rm JL} = 14\,{\rm K}$ for the dash-dotted curve. For the optimal value of the ratio $E_{\rm JL}/E_{\rm JS}$, denoted as $r_{\rm o}$, the dependence $E_{\rm J}(\varphi)$ becomes flat near $\varphi = 0$ at $\Phi = \Phi_0/2$ (solid curve). For smaller values of $E_{\rm JL}/E_{\rm JS}$, a double well potential is realized near full frustration. (c) "Phase diagram" of the ladders on the r-Φ plane. The values of $r_{\rm o}$ are 4.1 and 4.5 for the ladders with $N = 6$ and 24, respectively. The values of $r - r_{\rm o}$ for the studied devices are shown as horizontal lines.

perinductor and superinductor-based qubits is realized when the curvature $\partial^2 E_{\rm J}(\varphi)/\partial\varphi^2|_{\varphi=0}$ vanishes exactly at full frustration ($\Phi = \Phi_0/2$). Indeed, because the energy is an even function of the flux at full frustration, the device in this regime is insensitive in the first order to the flux noise [13]. This allows for simultaneous realization of the maximum inductance (i.e. the maximum fluctuations of the phase across the ladder) and the minimal coupling to the flux noise. This regime corresponds to the optimal value of the ratio $E_{\rm JL}/E_{\rm JS}$, which we denote as $r_{\rm o}$. The $r_{\rm o}$ value, calculated within the classical approximation ($E_{\rm C} = 0$), varies between 3 for a single unit cell and 5 for a very long ladder. Quantum fluctuations renormalize $E_{\rm J}(\varphi)$ and reduce $r_{\rm o}$ by δr; for our devices $\delta r \sim 0.5$-0.7.

We have experimentally studied two types of ladders with the number of unit cells $N = 6$ and 24. Short ladders with $N = 6$ allow for direct comparison between experimental data and simulations based on the numerical diagonalization of the system Hamiltonian. Because these simulations are infeasible for a larger number of unit cells, the ladders with $N = 24$ were treated within the quasi-classical approximation. These longer ladders demonstrate the potential of our novel approach: their microwave impedance exceeds $R_{\rm Q}$ by an order of magnitude.

The ladders and the readout circuits were fabricated using multi-angle electron-beam deposition of Al films through a lift-off mask (see Supplementary Materials IA for details). The in-plane dimensions of small and large junctions were $0.16 \times 0.16\,\mu{\rm m}^2$ and $0.30 \times 0.30\,\mu{\rm m}^2$, respectively. The unit cell size was $3 \times 5\,\mu{\rm m}^2$, and the flux $\Phi = \Phi_0/2$ was realized in the magnetic field $B \approx 0.7\,{\rm G}$.

The ladders parameters are listed in Table I. Several devices with systematically varied values of r were fabricated on the same chip and inductively coupled to the same microstrip line. The devices could be individually addressed due to their different resonance frequencies.

The effective kinetic inductance of the ladder, $L_{\rm K} = (\omega_{01}^2 C_{\rm K})^{-1}$, was calculated from the measured frequency ω_{01} of the $|0\rangle \leftrightarrow |1\rangle$ transition in the resonance circuit formed by the ladder and the interdigitated capacitor. The capacitance $C_{\rm K}$ is larger than the capacitance of the interdigitated capacitor due to the parasitic capac-

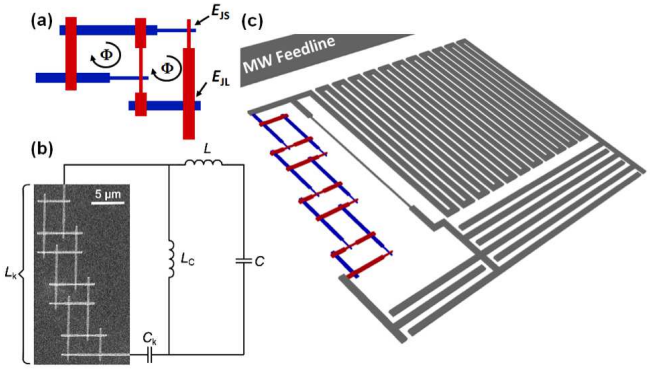

FIG. 2: (Color online) Schematic description of the on-chip circuit. (a) Topology of two unit cells of the ladder. The bottom electrodes are shown in blue, the top electrodes are shown in red. (b) The circuit diagram of the superinductor and LC resonators coupled via the kinetic inductance $L_{\rm C}$ of a narrow superconducting wire. The micrograph shows a ladder with six unit cells. (c) The on-chip circuit layout of two resonators inductively coupled to the microwave (MW) feedline.

TABLE I: Josephson junction parameters. E_{CS} and E_{CL} are the charging energies for the small and large junctions.

Device	Number of unit cells	E_{JS}, K	E_{CS}, K	E_{JL}, K	E_{CL} K	$r = E_{JL}/E_{JS}$	C_K, fF	L_C, nH	$L_K(\Phi = 0)$, nH	$L_K(\Phi = \Phi_0/2)$, nH
1	6	3.2	0.46	14.5	0.15	4.5	18	0.4	3.7	130
2	24	3.15	0.46	14.5	0.15	4.6	5	0.8	16	3 000

itance to the ground. The resonance frequency of this circuit, referred below as the superinductor resonator, varies with the magnetic field by an order of magnitude (see below), whereas the bandwidth of the cryogenic preamplifier and cold circulators in our measuring setup is limited to the range of 3-10 GHz (the microwave setup is described in Supplementary Materials IB). To overcome this limitation, the superinductor resonator was coupled to a linear lumped-element LC resonator with a resonance frequency $\omega_{LC}/2\pi \sim 7$ GHz via the coupling inductor L_C [a narrow superconducting wire, Figs. 2(b) and 2(c)]. The LC resonator is formed by an inductor (meandered 2-μm-wide Al wire) with $L = 5$ nH and an interdigitated capacitor (2-μm-wide fingers with 2 μm spacing between them) with $C = 100$ fF [Fig. 2(c)]. Both the superinductor and LC resonators are inductively coupled to a 2-port Al microstrip feedline with a 50 Ω wave impedance. When the superinductor resonator is excited by a second-tone microwave frequency ω_2, its impedance changes due to non-linearity; this results in a shift of the resonance of the LC resonator probed by the first-tone microwaves with $\omega_1 \approx \omega_{LC}$. The maximum shift occurs at the frequency $\omega_2 = \omega_{01}$ that corresponds to the $|0\rangle \leftrightarrow |1\rangle$ transition.

Figure 3 shows the resonance modes corresponding to the transition $|0\rangle \leftrightarrow |1\rangle$ in the superinductor resonators with the 6-cell and 24-cell ladders. The insets in Fig. 3 show the avoided crossing between the lowest modes of the superinductor and LC resonators observed in the first-tone measurements (these avoided crossings illustrate the strength of coupling between these resonators). The measured values of the lowest-mode frequency ω_{01} for the 6-cell ladder are in excellent agreement with simulations based on the numerical diagonalization of the circuit Hamiltonian (see Supplementary Materials IIB). The only fitting parameter in these calculations was the ratio $r = E_{JL}/E_{JS}$, which is within 15 % of the designed value. The nominal junction parameters for the 24-cell ladder also agree with the quasi-classical simulation of the dependence $\omega_{01}(\Phi)$.

Superinductor applications require that the frequency ω_{01}, which corresponds to the "global" mode of the superinductor, should be much smaller than the frequency of its internal excitations, ω_{int}. Far away from full frustration, the internal modes correspond to very high frequencies of an order of the Josephson plasma frequency (~ 100 GHz for our samples). At full frustration, ω_{int} decreases, but, according to our estimate, remains above

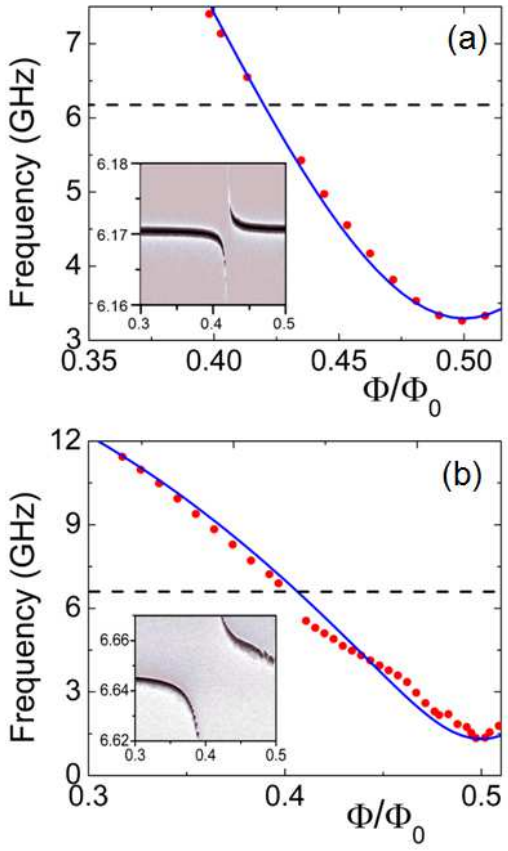

FIG. 3: (Color online) Spectroscopic data for the ladders with $N = 6$ (a) and $N = 24$ (b). The resonance frequencies $\omega_{01}(\Phi)/2\pi$ of the $|0\rangle \leftrightarrow |1\rangle$ transition measured in the second-tone experiments are shown by red dots. The horizontal dashed lines correspond to the resonance frequency of the LC resonators. The blue curves represent the fits based on numerical diagonalization of the circuit Hamiltonian for device 1 (a) and the quasi-classical modeling for device 2 (a); for the simulation parameters, see Table I. The grayscale insets show the microwave amplitude $|S_{21}|$ versus the first-tone microwave frequency $\omega_1/2\pi$ and the normalized flux Φ/Φ_0 measured near the avoided level crossings.

10 GHz for the 24-cell device.

The inductance at full frustration increases as r approaching its optimal value r_o, which depends on the number of unit cells (see Supplemental Materials IIB): $r_o = 4.1$ for $N = 6$ and $r_o = 4.5$ for $N = 24$. Even though both devices 1 and 2 have similar values of r (i.e. nominally identical junction parameters), their proximity

to the critical point is significantly different. For device 1 with $r - r_o \approx 0.4$, the inductance at full frustration exceeds that at zero field by a factor of 35. For device 2 with $r - r_o \approx 0.1$, this increase exceeds two orders of magnitude, and the inductance at full frustration is $3\,\mu$H (for comparison, this is the inductance of a 3-meter-long wire). The total capacitance of the superinductor resonator, $C_K = 5\,$fF (see Table I), includes the capacitance of the interdigitated capacitor (2 fF) and the parasitic capacitance of all wires and the superinductor to the ground (3 fF) obtained by circuit modeling. By "meandering" the ladder and shrinking the tested moderately-sized ($3 \times 5\,\mu$m^2) unit cell, the parasitic capacitance can be reduced down to $\sim$ 1 fF; the impedance of such a ladder approaches 50 kΩ at $\omega/2\pi =$ 3 GHz.

The nonlinearity of the superinductor-based qubit increases dramatically with approaching the optimal working regime ($r = r_o$ and $\Phi = \Phi_0/2$). According to our quantum simulations, the nonlinearity factor $\gamma = (\omega_{12} - \omega_{01})/\omega_{01}$ (ω_{12} is the frequency of the $|1\rangle \leftrightarrow |2\rangle$ transition) for the 24-cell ladder (device 2) with $r - r_o \approx 0.1$ approaches 40 % at full frustration. Strong, tunable quartic non-linearity of the studied superinductor is an asset for the qubit design. In particular, strong anharmonicity enables fast qubit operations and qubit readout due to a large energy difference between the $|0\rangle \leftrightarrow |1\rangle$ and $|1\rangle \leftrightarrow |2\rangle$ transitions [14].

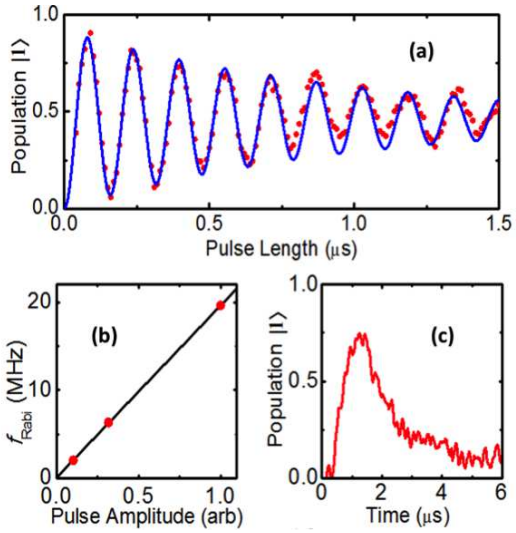

FIG. 4: (Color online) (a) Rabi oscillations of the population of the first excited level of the superinductor resonator in device 1. The phase shift of the LC resonance was measured while the superinductor resonator was excited by the second-tone pulsed microwaves with $\omega_2 = \omega_{01}$. The data are shown for the phase $\varphi = 2\pi\Phi/\Phi_0 = 0.94\pi$. The solid line represents the fit with the Rabi decay time 1.4 μs. (b) Dependence of the Rabi frequency on the amplitude of microwaves with $\omega_2 = \omega_{01}$. (c) The response of the LC resonator (measured at $\omega_1 = \omega_{LC}$) to the excitation of the superinductor resonator by a 0.4 μs second-tone pulse.

In order to demonstrate the high quality of our superinductor, we have measured Rabi oscillations in the qubit formed by the superinductor and the capacitor C_K [Fig. 4(a)]. In these measurements, we have monitored the phase shift of the LC resonance while the superinductor resonator was excited by pulsed microwaves with $\omega_2 = \omega_{01}$. The quantum nature of these oscillations was verified by observing the linear dependence of the Rabi frequency on the amplitude of the microwave field [Fig. 4(b)]. The observed decay time of Rabi oscillations exceeded 1 μs and was limited by the energy relaxation time [cf. Fig. 4(c)]. The dominant source of energy relaxation is the intentional inductive coupling to the LC resonator and the microwave feedline.

The intrinsic decoherence rate of the qubit is expected to be very low. Because the curvature $\partial^2 E_J(\varphi)/\partial\varphi^2$ (which controls the position of energy levels) has a minimum at full frustration, one expects that the flux noise does not affect the qubit in the linear order. Another common source of dephasing in a chain of superconducting islands coupled by Josephson junctions is the phase-slip processes in combination with ubiquitous fluctuations of offset charges on the islands [15]. Due to the Aharonov-Casher effect [3, 16–18], these two factors result in the decoherence which is directly proportional to the phase slip rate. In the studied devices this rate, being proportional to $\exp[-c(E_{JL}/E_{CL})^{1/2}]$, where $c \approx 2.5$-2.8, is expected to be negligible due to a large ratio E_{JL}/E_{CL} (≈ 100) for the junctions that form the ladder backbone [Fig. 1(a)].

We envision many applications for the designed superinductor: this element has the potential to reduce the charge noise sensitivity of Josephson qubits, enable implementation of the fault tolerant qubits, and provide sufficient isolation for the electrical current standards based on Bloch oscillations. The ability to transform this element from an inductor with an almost linear response into a very non-linear superinductor by tuning the magnetic field can facilitate controllable coupling between qubits. In a moderately or strongly non-linear regimes, the superinductor-based resonator can also operate as a qubit with a low decoherence rate. Being combined with a small Josephson junction, the superinductor can be used as an adiabatic switch — an element whose impedance changes exponentially with magnetic field [5, 19], which is crucial for the fault tolerant qubit operations [6].

We would like to thank V. Manucharyan and A. Zamolodchikov for helpful discussions. The work was supported by DARPA (HR0011-09-1-0009), NSF (DMR 1006265), and ARO (W911NF-09-1-0395).

[1] K.K. Likharev and A.B. Zorin, J. Low Temp. Phys. **59**, 347 (1985).

[2] D.V. Averin and K.K. Likharev, *Single Electronics: a correlated transfer of single electrons and Cooper pairs in systems of small tunnel junctions*, in *Mesoscopic Phenomena in Solids*, Eds. B.L. Altshuler, P.A. Lee, and R.A. Webb (Elseiver 1991), pp.173-271.

[3] V.E. Manucharyan, J. Koch, L.I. Glazman, and M.H. Devoret, Science **326**, 113 (2009).

[4] V. Manucharyan, Ph.D. Thesis (Yale University, 2012).

[5] A. Kitaev, arXiv:cond-mat/0609441 (2006).

[6] B. Doucot and L.B. Ioffe, Rep. Prog. Phys. **75**, 072001 (2012).

[7] R.P. Feynman, R.B. Leighton, and M. Sands, *The Feynman Lectures on Physics* (Addison-Wesley, Reading, MA, 1964), Vol. 2, Ch. 23.

[8] M. Tinkham, *Introduction to Superconductivity* (McGraw-Hill Book Co, New York, 1996).

[9] M. Watanabe, Phys. Rev. B **69**, 094509 (2004).

[10] S. Corlevi, W. Guichard, F.W.J. Hekking, and D.B. Haviland, Phys. Rev. Lett. **97**, 096802 (2006).

[11] A.J. Annunziata *et al.*, Nanotechnology **21**, 445202 (2010).

[12] J. Ku, V. Manucharyan, and A. Bezryadin, Phys. Rev. B **82**, 134518 (2010).

[13] D. Vion *at al.*, Science **296**, 886 (2002).

[14] A.B. Zorin and F. Chiarello, Phys. Rev. B **80**, 214535 (2009).

[15] V.E. Manucharyan *et al.*, Phys. Rev. B **85**, 024521 (2012).

[16] W.J. Elion *et al.*, Phys. Rev. Lett. **71**, 2311 (1993).

[17] I.M. Pop *et al.*, Phys. Rev. B **85**, 094503 (2012).

[18] J. Koch *et al.*, Phys. Rev. Lett. **103**, 217004 (2009).

[19] K.A. Matveev, A.I. Larkin, and L.I. Glazman, Phys. Rev. Lett. **89**, 096802 (2002).